*Geophys. J. Int.* (1999) **137,** 91–106

# Imaging upper-mantle discontinuity topography using underside-reflection data

Filip Neele* and Han de Regt

*Department of Theoretical Geophysics, Utrecht University,* PO Box 80021, 3508 *TA Utrecht, the Netherlands*

Accepted 1998 October 16. Received 1998 July 31; in original form 1997 May 19

## SUMMARY

This paper presents a method to invert underside-reflection ($P_dP$ or $S_dS$ arrivals) data for lateral depth variations of upper-mantle discontinuities, combining traveltime and amplitude data. The method greatly improves the resolution of small-scale undulations obtained by existing imaging methods and does not su er from the long-wavelength biases that are likely to be present in currently available models. Existing inversion methods account for the large size of the Fresnel zone of underside reflections, but not for its complexity, arising from the mini-max traveltime nature of *PP*- and *SS*-related waves. This neglect results in long-wavelength artefacts from small-scale undulations of the discontinuities, obscuring true long-wavelength depth variations. The inversion method presented in this paper uses a complex-valued sensitivity kernel, derived from the representation of underside reflections through a Kirchho integral formulation. The sensitivity kernel accounts for the varying sensitivity of the waveforms to discontinuity structure over the Fresnel zone. The method is applied to a large, synthetic data set. The data set consists of $P_dP$ amplitudes and traveltimes. The results show that the new inversion method resolves depth variations on a lateral scale that is smaller than the size of the Fresnel zone of individual underside reflections (but larger than the dominant wavelength), retaining the resolution of large-scale variations. The results presented here suggest that the discontinuity depth variations induced by slab penetration of the 670 discontinuity could be resolved by current broad-band $P_{670}P$ data sets.

**Key words:** 410 discontinuity, 670 discontinuity, upper mantle.

## 1 INTRODUCTION

Current maps of long-wavelength variations of the depths of the discontinuities (Shearer 1991; Shearer & Masters 1992; Shearer 1993; Gossler & Kind 1996) reveal undulations with wavelengths of several thousands of kilometres and peak-to-peak amplitudes of 20–30 km. Such maps provide important insights into horizontal temperature gradients in the Earth and can be used in the modelling of convection process (for example Phipps-Morgan & Shearer 1993; Forte & Woodward 1997). These maps have been obtained from di erential $SS$–$S_dS$ traveltimes, using ray theory to relate traveltime perturbations to reflector depth at the $S_dS$ bounce point. However, Neele, de Regt & VanDecar (1997) showed that the inversion method used to convert the $SS$–$S_dS$ traveltimes to discontinuity depth is flawed, as the complex structure of the Fresnel zone of the underside reflections is ignored.

This paper presents a method that does not su er from these drawbacks. The method uses the traveltime and amplitude of *PP*- or *SS*-precursors to reconstruct lateral depth variations of the upper-mantle discontinuities. The method accounts for the Fresnel zone of underside reflections and their mini-max traveltime nature.

The problem of obtaining interface geometry from waves interacting with the interface has been the subject of various studies, and has close links with migration methods used in exploration seismics. Nowack & Lyslo (1989) presented a method to resolve interface geometry from reflected waves. These authors used ray theory to relate amplitude and traveltime variations to interface topography, ignoring the finite extent of the Fresnel zone. The method presented here is a backprojection of the observed wavefield onto a single 2-D slice through the 3-D Fresnel volume that surrounds the ray-geometrical path. In that sense, the method can be viewed as

* Now at: TNO Physics and Electronics Laboratory, PO Box 96864, 2509 JG, The Hague, The Netherlands.

a simplified version of more elaborate migration and imaging methods that take the full Fresnel volume into account (see, for example, Woodward 1992; Luo & Schuster 1991; Doornbos 1992; Vasco & Majer 1993).

In the next section, the sensitivity kernel of underside reflections is derived and the inverse problem is formulated. Then, a number of synthetic experiments are presented, on both simple and more realistic data sets. The emphasis lies on subducting-slab-induced discontinuity depth variations. The examples illustrate the problems associated with the straightforward, ray-theory-based interpretation of underside-reflection traveltimes and show the high resolution that can be obtained from current underside-reflection data sets if the proper sensitivity kernel for discontinuity structure is used.

## 2 INVERSION METHOD FOR UNDERSIDE REFLECTION DATA

The inverse procedure presented here is based on the Kirchho –Helmholtz integral representation of a wavefield. This integral method has been widely used to synthesize the wavefield in laterally varying media (for example Sen & Frazer 1987; Kampfmann & Muller 1989; Neele & Snieder 1992; Van der Lee, Paulssen & Nolet 1994; Schimmel & Paulssen 1996; Neele *et al.* 1997). It is especially useful for the present case of reflection by an undulating interface, as scattering and focusing are automatically taken into account. In the following, the frequency-domain formulation for an elastic medium given by Frazer & Sen (1985) and Frazer (1987) is used as starting point. Symbolically, the spectrum of an underside reflection $P_dP$ can be written as

$$P_dP^{(0)}(\omega) = i\omega P(\omega) \int_\Sigma \frac{1}{G_1} \exp(i\omega T_1) R \frac{1}{G_2} \exp(i\omega T_2)\, d\Sigma, \qquad (1)$$

where $P(\omega)$ is the spectrum emitted by the source; $G_1$ and $G_2$ represent the geometrical spreading from the source to the point of reflection and from there to the receiver, respectively; and $R$ is the generalized elastic reflection coe cient (Frazer & Sen 1985). The integration in (1) is over the discontinuity $\Sigma$; the radiation pattern from the source may be included in the spreading term $G_1$. $T_1$ and $T_2$ are the traveltimes along the first and second legs of $P_dP$. The factor $i\omega$ corrects for the low-pass character of the integration. It should be noted here that the notation $P_dP(\omega)$ is used to include both *PP* and *SS* precursors: expression (1) is valid for both *PP* and *SS* and their related underside reflections at the upper-mantle discontinuities if the appropriate spreading terms, traveltimes and generalized reflection coe cients are used in the evaluation of (1).

As noted by Ringdal *et al.* (1972), it is appropriate to handle amplitudes in the log domain, as the various mechanisms a ecting amplitudes act in multiplicative fashion. In the log domain, contributions from, for example, source and station e ects may simply be subtracted from the amplitude signal. For this reason, the logarithm of both sides of expression (1) is taken. This separates amplitude and phase in the spectrum into the real and imaginary parts of the expression. Perturbation theory can then be used to find the first-order change in the spectrum $P_dP^{(0)}(\omega)$ due to small changes $\delta h$ in the depth of the discontinuity $\Sigma$. This first-order spectrum perturbation is given by

$$\log(P_dP^{(1)}(\omega)) \approx \log\left( P_dP^{(0)}(\omega) + \frac{\partial P_dP(\omega)}{\partial h}\delta h \right)$$

$$\approx \log(P_dP^{(0)}) + \frac{1}{P_dP^{(0)}} \frac{\partial P_dP(\omega)}{\partial h}\delta h, \qquad (2)$$

where it is understood that $\delta h$ is a function of both latitude and longitude. For small perturbations in reflector position, the first-order perturbation in the spectrum is obtained by assuming that the dominant contribution to the spectrum perturbation occurs through the traveltime $T$. It is assumed that a small change in the position of the reflector has a second-order e ect on the generalized reflection coe cient and geometrical spreading functions. For teleseismic *PP* or *SS* and related waves, this is a reasonable assumption. With this assumption, the spectrum perturbation in (2) can be written as

$$\frac{1}{P_dP^{(0)}} \frac{\partial P_dP(\omega)}{\partial h}\delta h \approx -\omega^2 \frac{P(\omega)}{P_dP^{(0)}} \int_\Sigma \frac{R}{G_1 G_2} \exp(i\omega T) \frac{\partial T}{\partial h}\delta h\, d\Sigma, \qquad (3)$$

where $T = T_1 + T_2$. In (3), the traveltime perturbation is $\delta T = (\partial T/\partial h)\delta h$. Rodgers & Wahr (1994) give a derivation of the term $\partial T/\partial h$ for underside reflections. Expression (3) gives a linear, first-order relation between spectrum perturbations and depth variations of the interface $\Sigma$.

For (3) to be used in an inversion of observed spectrum perturbations for reflector depth variations (a back-projection of spectral misfits onto interface depth perturbations $\delta h$), the integration over $\Sigma$ must be limited to a finite region. A natural choice would be to limit the integration to an area containing the first or first few Fresnel zone(s). To reduce the error introduced by such a cut-o of the integration, the method of Snieder & Lomax (1996) is followed. The right-hand side in (3) is multiplied and divided by a function $W(\omega)$,

$$W(\omega) = \int_\Sigma \frac{R}{G_1 G_2} \exp(i\omega T)\, d\Sigma, \qquad (4)$$

which represents the $P_dP$ sensitivity kernel for the reference medium, integrated over the reflector $\Sigma$. The spectrum perturbation (3) then becomes

$$\frac{1}{P_dP^{(0)}} \frac{\partial P_dP}{\partial h}(\omega)\delta h = \frac{i\omega \int_\Sigma \frac{R}{G_1 G_2} \exp(i\omega T) \frac{\partial T}{\partial h}\delta h\, d\Sigma}{\int_\Sigma \frac{R}{G_1 G_2} \exp(i\omega T)\, d\Sigma}, \qquad (5)$$

where use has been made of the fact that $i\omega P^{(0)}(\omega)W(\omega) = P_dP^{(0)}$, according to (1), which cancels the factor $P_dP^{(0)}(\omega)$ that is present in the denominator in (3). Now the integration over $\Sigma$ in the two remaining integrals in (5) is limited to a region containing the first (or first few) Fresnel zone(s). Expression (5) then becomes

$$\frac{1}{P_dP^{(0)}} \frac{\partial P_dP(\omega)}{\partial h}\delta h = \frac{i\omega \int_{FZ} \frac{R}{G_1 G_2} \exp(i\omega T) \frac{\partial T}{\partial h}\delta h\, d\Sigma}{\int_{FZ} \frac{R}{G_1 G_2} \exp(i\omega T)\, d\Sigma}, \qquad (6)$$

where *FZ* indicates the region containing the first Fresnel zone. It was shown by Groenenboom & Snieder (1995) and

Snieder & Lomax (1996) that the errors associated with the cut-o in the integration are small and that for smooth media (6) is a good approximation of (3).

With the first-order spectrum perturbation given by (6), the inverse problem can be formulated. The data are amplitude $A_{\rm obs}$ and traveltime $T_{\rm obs}$, possibly as a function of frequency. Thus, the misfit between observed and reference spectra becomes

$$\begin{aligned}&\log(A_{\rm obs}\exp(i\omega T_{\rm obs}))-\log(A_{\rm ref}\exp(i\omega T_{\rm ref}))\\&\quad=\log(A_{\rm obs})-\log(A_{\rm ref})+i\omega(T_{\rm obs}-T_{\rm ref})\\&\quad=\frac{1}{A_{\rm ref}\exp(i\omega T_{\rm ref})}\frac{\partial P_dP(\omega)}{\partial h}\delta h,\end{aligned}\tag{7}$$

where the replacement $P_dP^{(0)}=A_{\rm ref}\exp(i\omega T_{\rm ref})$ has been made. Dividing the surface $\Sigma$ into cells, the integration in (6) transforms into a sum. Using this and dividing (7) into real and imaginary parts, the formulation for the inverse problem is obtained:

$$\Delta\log A=\log(A_{\rm obs})-\log(A_{\rm ref})=\mathscr{R}e\left(\sum_j\frac{\partial F}{\partial h_j}\right)\delta h_j,\tag{8a}$$

$$\omega\Delta T=(T_{\rm obs}-T_{\rm ref})=\mathscr{I}m\left(\sum_j\frac{\partial F}{\partial h_j}\right)\delta h_j.\tag{8b}$$

The Frechet derivatives $\partial F/\partial h$ in (8) are given by

$$\begin{aligned}\frac{\partial F}{\partial h_j}=i\omega&\left(\int_{FZ}\frac{R}{G_1G_2}\exp(i\omega T)\,d\Sigma\right)^{-1}\left(\frac{R}{G_1G_2}\right)_j\\&\times\exp(i\omega T_j)\frac{\partial T_j}{\partial h_j}dO_j,\end{aligned}\tag{9}$$

where $R$, $G_1$, $G_2$ and $T_j$ are the generalized reflection coe cient, geometrical spreading terms and traveltime for a ray from the source via cell $j$ to the receiver, respectively; and $dO_j$ is the surface of the cell.

The inverse procedure of mapping spectrum misfits into discontinuity-depth perturbations can now be written as a matrix equation. A smoothness criterion is added to regularize the solution. As the inversions with synthetic data shown below are performed to test the power of $P_dP$ data to resolve small-scale depth variations of the discontinuities, the second derivative of depth perturbations in both latitude $\theta$ and longitude $\phi$ is damped. The combined system to be solved is then

$$\begin{pmatrix}\gamma_{\rm A}\mathbf{F}_{\rm a}\\ \gamma_{\rm T}\mathbf{F}_{\rm t}\\ \gamma\partial_\theta^2\\ \gamma\partial_\phi^2\end{pmatrix}\delta\mathbf{h}=\begin{pmatrix}\gamma_{\rm A}\Delta\log\mathbf{A}\\ \omega\gamma_{\rm T}\Delta\mathbf{T}\\ 0\\ 0\end{pmatrix},\tag{10}$$

where $\mathbf{F}_{\rm a}$ and $\mathbf{F}_{\rm t}$ are the matrices containing the Fréchet derivatives for amplitude and traveltime (from eqs 9a and b). $\Delta\log\mathbf{A}$ and $\Delta\mathbf{T}$ are the (log-)amplitude and traveltime misfits, respectively. The parameter $\gamma$ controls the trade-o between data fit and model smoothness,while $\gamma_{\rm A}$ and $\gamma_{\rm T}$ weigh amplitude and traveltime data, respectively. The standard errors for amplitude data are often much larger than those for traveltimes (for example Neele *et al.* 1993b), suggesting a di erential weight derived from the relative standard errors. In the results presented below, $\gamma_{\rm A}$ and $\gamma_{\rm T}$ are chosen in such a way that amplitude and traveltime data have equal rms misfit before the inversion. The system (10) is solved in a least-squares sense using the routine LSQR of Paige & Saunders (1982).

It follows from eqs (8a), (8b) and (9) that (to first order) the traveltime derivatives with respect to discontinuity depth behave as $\cos\omega\Delta T_j$, with $\Delta T_j$ the traveltime di erence between Snell's ray (the geometrical ray path in the reference model) and the ray path via cell $j$. Hence, the traveltime Fréchet derivatives have constant sign across the first Fresnel zone, as would be expected. An overall elevation of the discontinuity would then induce a traveltime perturbation in agreement with the ray-geometrical derivative $\partial T/\partial h$. The amplitude Fréchet derivatives, on the other hand, behave as $\sin\omega\Delta T_j$ [note the factor $i$ in expression (9)], and hence change sign across the Fresnel zone. The saddle shape of the traveltime function (see Fig. 1) causes these Fréchet derivatives to change sign across the first Fresnel zone. A constant elevation of the discontinuity would induce zero amplitude perturbation. To first order this is correct, as the dominant e ect of such an elevation is to delay the wavefield, rather than a ect the amplitude. It follows from the $\sin\omega\Delta T_j$ behaviour of the amplitude Fréchet derivatives that the structure that best focuses the $P_dP$ wavefield at the receiver is also saddle-shaped. A 2-D stationary-phase approximation (Bleistein 1984) of (1) proves that the highest $P_dP$ amplitudes occur when the second spatial derivatives of the traveltime function at the reflection point are near zero; a saddle-shaped discontinuity can (locally) reduce the curvature of the traveltime function to zero. The results of Davis *et al.* (1989) are in agreement with this behaviour of the amplitude Fréchet derivatives. These authors showed that a downward deflection of the discontinuity along the source–receiver great circle focuses $P_dP$ energy; in contrast, perpendicular to the great circle, upward deflections of the discontinuity best focus $P_dP$ energy. The combination of these two structures forms a saddle.

If the discontinuity structure is such that the second spatial deviatives of the traveltime function are small over a su ciently large area in a part of the wavefield far from the geometrical bounce point, the resulting arrival in the seismogram may have a strongly deviating traveltime and a large amplitude. Such an arrival could then easily be mistaken for an underside reflection from a discontinuity at an abnormal depth. Examples presented below (Section 3.2) show that such arrivals may be present in real data.

Owing to the approximation in (2), the above formulation is valid for small perturbations of the traveltime $T$. However, it allows for a relatively simple non-linear iteration, as the Fréchet derivatives can be computed for any non-plane, but smooth, interface geometry. Here, smooth means that the curvature of the interface must be much larger than the wavelength of waves used (Frazer & Sen 1985). Non-linearities due to large traveltime perturbations relative to a laterally plane reference model may thus be handled in an iteratively non-linear inversion, updating the Fréchet derivatives after every linear inversion step.

The above procedure maps misfits between observed and reference spectra onto lateral variations of the interface $\Sigma$. In eq. (8), however, the dependence of spectral amplitude $A$ on frequency has been silently dropped. The reason is that it is extremely di cult to observe individual underside reflections in single seismograms (for example Shearer 1990; Neele & Snieder 1992; Gossler & Kind 1996), and $P_dP$ spectra cannot

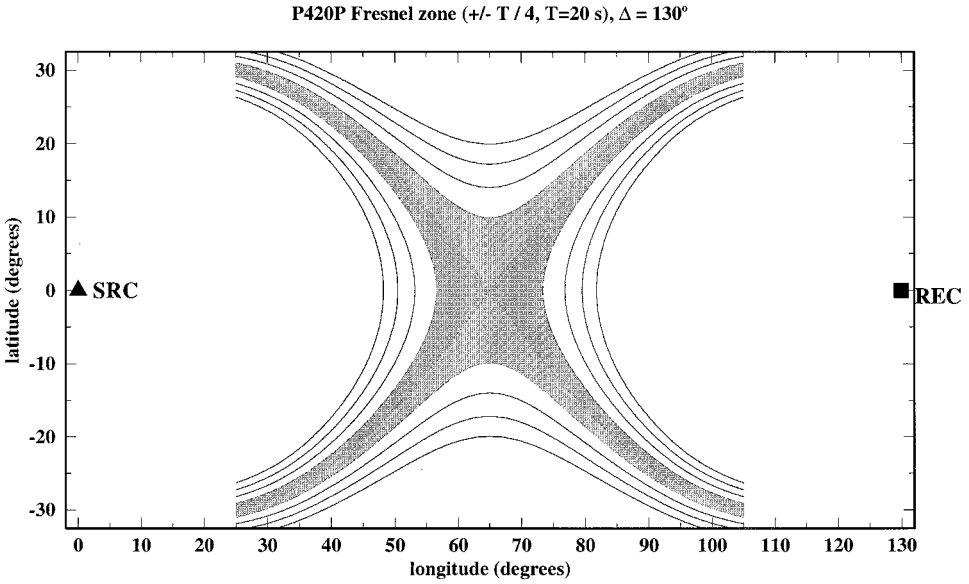


**Figure 1.** Fresnel zone of a 20-s $P_{420}P$ wave at an epicentral distance of 130°, projected on the 420-km discontinuity. The Fresnel zone is defined by plus or minus a quarter of the period traveltime di erence from the ray-geometrical path; the ray-geometrical bounce point is at the centre of the shaded region. The dark-shaded region corresponds to energy within the Fresnel zone arriving ahead of the ray-geometrical arrival, while light shades indicate later-arriving parts of the wavefield.

be obtained directly from the data. Therefore, an additional simplification is made. As long-period data have a rather narrow frequency band, it is assumed that the spectrum $P_dP(\omega)$ can be estimated using $A_{\rm obs}\exp(i\omega T_{\rm obs})$, where $A_{\rm obs}$ and $T_{\rm obs}$ are the observed amplitude and arrival time, respectively, of a $P_dP$ or $S_dS$ wave, and $\omega$ is the dominant frequency in the data. Amplitudes $A_{\rm obs}$ and $T_{\rm obs}$ can be obtained from cross-correlation of the seismogram with the *PP* or *SS* waveform, as done by Shearer (1991, 1993). In that case, data are defined relative to the *PP* or *SS* wave.

For long-period $S_dS$ data, the dominant frequency is 25–30 s. In the computations below, long-period $P_dP$ waves are used with a dominant frequency of 15–20 s, which have about the same wavelength and Fresnel-zone size as 30-s $S_dS$ waves. The Fresnel zone of a 20-s $P_{420}P$ wave at an epicentral distance of 130° is shown in Fig. 1. The Fresnel zone is defined by a maximum traveltime di erence with the geometrical ray path (Snell's ray) of plus or minus a quarter of the period. The Fresnel zone is about $20^\circ \times 20^\circ$ wide, centred around the geometrical ray path. The four long tails are a result of the minimax nature of the traveltime function. Owing to the large size of the Fresnel zone, topographic structure on the discontinuity far from the geometrical bounce point may a ect the waveform.

To perform the inversion, the discontinuity surface is divided into rectangular, non-overlapping cells. The size of the cells is approximately $2^\circ \times 2^\circ$, with a total of 10 318 cells completely covering the globe. The cell size is appropriate for the average bounce-point spacing in the realistic data used below. The cell size should be determined by the spacing of individual bounce-point locations, rather than the Fresnel zone of the waves, but should not be chosen smaller than the dominant wavelength in the data.

## 3 INVERSIONS WITH SYNTHETIC DATA

The method presented in the previous section is applied to a number of synthetic data sets, both to test the method and to show the small-scale lateral depth variations of the discontinuity that can be resolved using currently available long-period underside-reflection data. First, a simple model of expected discontinuity-depth variations near a single subducting lithospheric slab is considered. Inversions are performed with synthetic data sets of both $P_{420}P$ and $P_{670}P$ reflections. Then, synthetic data sets are generated for a global model of subduction zones. Inversions show the resolving power of current large data sets. Finally, the method is tested on a model with both large- and small-scale discontinuity-depth variations.

Synthetic underside reflection waveforms are computed using a Kirchho –Helmholtz method (for example Frazer & Sen 1985; Frazer 1987), which takes into account di raction e ects due to reflection o curved interfaces. The reader is referred to Neele & Snieder (1992) for more details about the computation of $P_dP$ synthetics. Traveltime and amplitude variations are obtained from a multi-channel cross-correlation procedure (VanDecar & Crosson 1990). Amplitudes are defined as baseline-to-peak amplitude of the cycle containing the time pick. No *PP* waveform is computed; the waveform cross-correlation is performed with the $P_dP$ waveforms only.

### 3.1 Simple small-scale topography

The model used is a simplified model of expected discontinuity-depth variations near a subducting slab, shown in Fig. 2. The model of Hel rich *et al.* (1989), adapted for a vertically descending slab, predicts a bell-shaped uplift of the 420-km discontinuity, with a width (at half-height) of about 2° and a maximum height of 50 km at the centre of the slab. Here, a cosine-squared function is used to model the uplift. The length of the subducting slab is 40°; a (cosine-squared) taper is applied to 2° from both ends.

Figs 3(a) and (b) show apparent depths and amplitude data obtained for the model in Fig. 2, plotted at the ray-geometrical

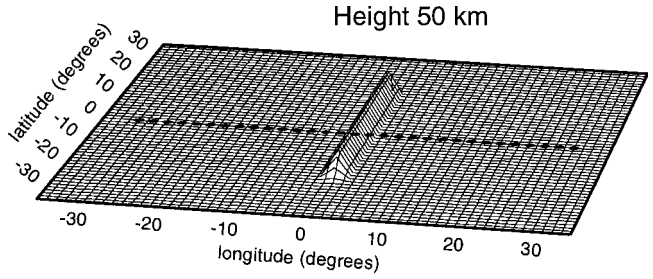


**Figure 2.** Model of discontinuity topography inside and near a subducting slab crossing the phase transition at 420 km depth. The $\cos^2$-function has a width (between zero crossings) of 4°; the maximum uplift at the centre of a slab is 50 km; The topography for the 670-km discontinuity is the same, except that in that case the discontinuity is deflected to greater depths.

bounce-point locations. Bounce points are spaced at 2° intervals, in both latitude and longitude, in the box (−30°, 30°) in latitude, (−30°, 30°) in longitude. Epicentral distance is fixed at 110°; for each source–receiver combination, the great circle is parallel to the longitude axis in Fig. 3. For this model and source–receiver geometry, Neele *et al.* (1997) show a number of synthetic seismograms that contain energy di racted by the slab-induced uplift of the discontinuity. Also shown in Figs 3(a) and (b) is the 10-km contour of the slab-induced structure. The apparent discontinuity depths in Fig. 3(a) have been converted from the traveltime perturbations, using ray theory to relate early (late) arrivals to a locally deeper (shallower) discontinuity at the ray-geometrical bounce point. Although this simple conversion is incorrect as it ignores the mini-max nature of the wave, it simplifies the interpretation of the traveltime data. Note that for $P_{420}P$ bounce points near the centre of the slab-induced structure, the apparent and true depth perturbations have opposite sign, and that strong side lobes exist for bounce points that are about 6°–8° away from the centre of the slab. The amplitude pattern in Fig. 3(b) shows lower amplitudes for bounce points near the centre of the slab, and high amplitudes for bounce points about 10° away from the slab. The former is due to defocusing and scattering by the relatively narrow slab-induced structure, whereas the latter can be explained by energy di racted from the slab and arriving at the same time as energy travelling along the ray-geometrical path.

Fig. 4 shows the trade-o curves between data misfit and model smoothness (circles in Fig. 4), using a 1-D model as reference. Amplitudes and traveltimes have similar initial rms misfits before the inversion. In the inversion the actual traveltime perturbations were used, not the apparent depths from Fig. 3(a). The choice of models shown below was based on the point along the trade-o curves where further data misfit reduction started to induce a large increase in model roughness, rather than on an optimum combination of model roughness and data misfit. All models shown here for the single-slab geometry have similar model roughness.

The model indicated by the solid circle in Fig. 4 is shown in Fig. 5. In the inversion the position of the local elevation of the discontinuity is reconstructed well, although some artefacts from the finite data set appear in the result. The height of the discontinuity uplift is not recovered in the inversion. The true height is 50 km, whereas only 15 km is found in Fig. 5. The locations of the cells used in the model parametrization do not coincide with the bounce-point locations in Figs 3(a) and (b). This causes an apparent curve in the reconstructed discontinuity topography.

Fig. 6 shows the results for a slab-induced deflection of the 670-km discontinuity. The model shown is represented in Fig. 4

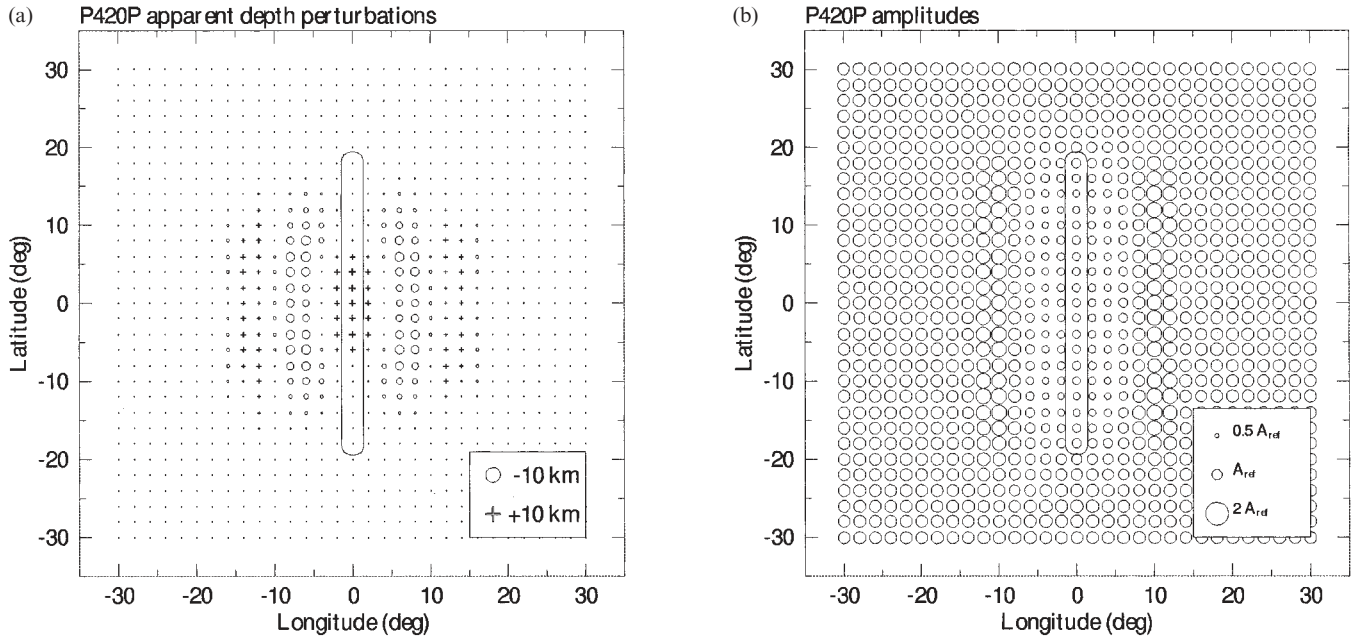


**Figure 3.** (a) Apparent discontinuity-depth perturbations obtained from $P_{420}P$ traveltimes, plotted at the ray-geometrical bounce points. Source–receiver great circles run parallel to the longitude axis; the epicentral distance is always 110°. The slab-induced structure is outlined by the +10 km contour. Note the presence of both positive and negative apparent depth perturbations. Apparent depth perturbations range from −6.5 to 4.5 km. (b) $P_{420}P$ amplitude variations, plotted at the bounce-point positions. Low amplitudes are found near the slab (defocusing), higher amplitudes about 10° from the slab (constructive interference $P_{420}P$ wave with slab di raction).

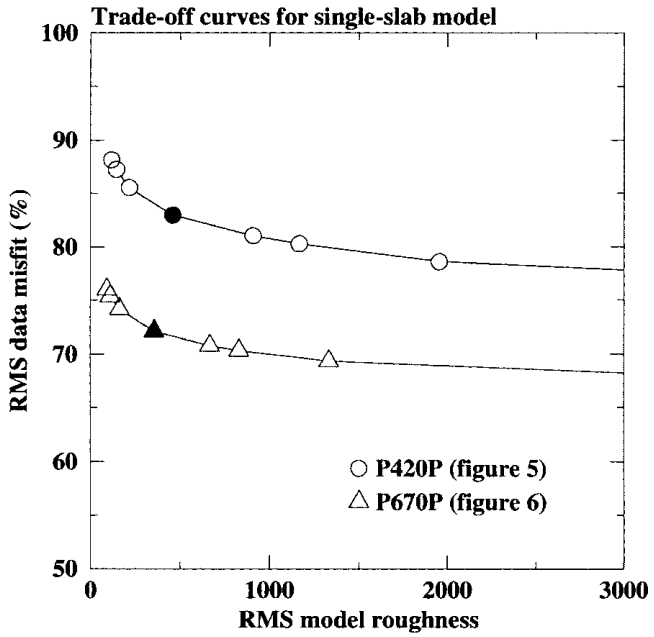


**Figure 4.** Trade-o curves for model smoothness and data misfit, for $P_{420}P$ (circles) and $P_{670}P$ data (triangles). The solid symbols represent the models shown in Figs 5 and 6.

by the solid triangle. The phase transition expected to occur at this depth is moved to greater depth inside a subducting slab. The model used to generate synthetic data has the same dimensions as the structure in Fig. 2, except that the amplitude of the deflection is +50 km. This is a reasonable value, based on results from high-p,T experiments on mineral assemblages (Ito & Takahashi 1989). A displacement of several tens of kilometres near subducting slabs has been observed using short-period arrays (for example Vidale & Benz 1992; Niu & Kawakatsu 1995; Collier & Hel rich 1997). The results from the inversion (Fig. 6) show that again the location and the sign of the depth perturbations are resolved. As in Fig. 5, the absolute value of the depth perturbations is not reconstructed in Fig. 6.

The inversion result in Figs 5 and 6 show that underside-reflection data can resolve the correct sign of small-scale deflections of the discontinuity, even though the greater part of the wavefield that hits the structure on the discontinuity is scattered and lost.

It cannot be expected that the true height of the elevation will be recovered, because the data do not contain direct information about this aspect of the model. Di ractions from the slab-induced topography are too small to dominate the $P_dP$ signal. In other words, those parts of the $P_dP$ wavefield that hit the small-scale structure in Fig. 2 are essentially scattered away; the $P_dP$ wave observed at the station carries

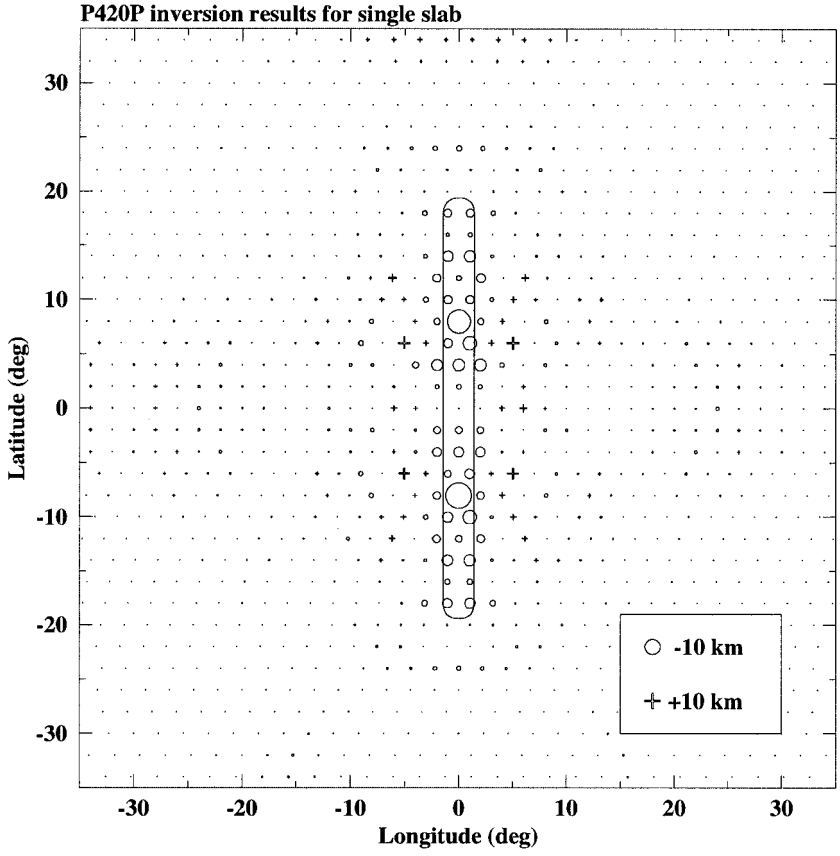


**Figure 5.** Result of inverting the $P_{420}P$ traveltime and amplitude data in Fig. 3. This model is represented by the solid circle in Fig. 4. The −10 km contour outlines the true discontinuity topography. Depth variations in the model are between −11 and 5 km.

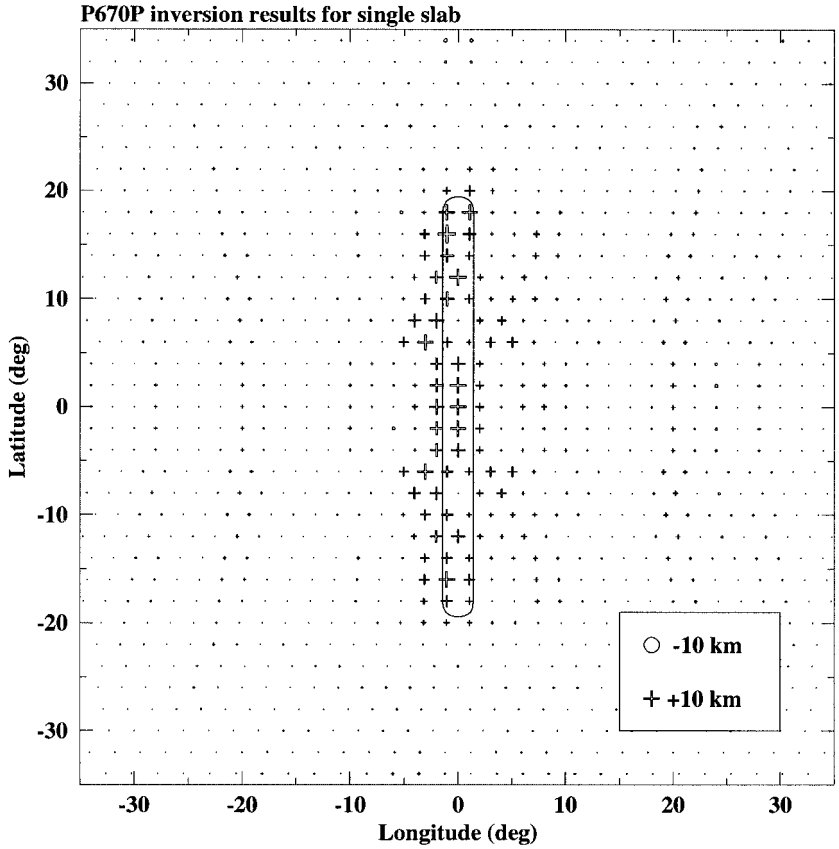


**Figure 6.** As Fig. 5, now for $P_{670}P$ data. Depth variations in the model are between $-3$ and 10 km.

information only about the position and sense of the elevation (that is up or down), but not about the absolute value of the elevation.

The slight asymmetry of the models in Figs 5 and 6 is due to the asymmetry in the Fréchet derivatives. This is caused by the receiver operator (projection on the vertical), which is larger for $P_dP$ rays with bounce points nearer to the source. The models in Figs 5 and 6 have slightly larger values for cells that are closer to the source [which is at (lon, lat) $= (-55^\circ, 0^\circ)$]. This also creates an apparent meandering of the reconstructed elevation in Fig. 6, where the varying discontinuity-depth perturbation with latitude is a result of the finite data set.

It should be emphasized that the lateral dimensions of the slab-induced structure in Figs 5 and 6 are much smaller than the size of the Fresnel zone of 20-s $P_{420}P$ or $P_{670}P$ waves (but larger than the dominant wavelength). Each $P_dP$ wave contains information about the average structure in its Fresnel zone, but it is the di erence between $P_dP$ waves from closely spaced bounce points that provides the information about small-scale lateral variations in discontinuity properties.

The inversion results shown in Figs 5 and 6 were obtained with all great-circle paths perpendicular to the discontinuity perturbation. Two additional tests show the resolution that can be obtained with great-circle paths parallel to the subducting slab and with a combination of parallel and perpendicular great-circle paths. Both tests are shown for the 670-km discontinuity, but similar results were obtained using $P_{420}P$ data.

Fig. 7 shows the results for the same set-up as used in Fig. 6, except that the discontinuity perturbation is rotated over 90°. Both position and extent of the structure are well resolved. This improvement over the results shown in Fig. 6 can be explained by the relative orientation of great circles and discontinuity structure. Wave energy scattered by the discontinuity perturbation is now scattered in the direction of the receiver, whereas in the set-up used for Figs 5 and 6 the scattered wavefield is not directed towards the receiver. This set-up of great-circle paths does not resolve the width of the perturbation as well as in Fig. 5, although the di erence is small. The reconstruction shown in Fig. 7 does not exhibit significant amplitude variation along its extent. Such variations are present in Fig. 5, where they are probably caused by the relative location and orientation of the discontinuity structure, bounce points and source–receiver great circles.

Fig. 8 shows the result obtained with great-circle paths both parallel and perpendicular to the discontinuity perturbation. The perturbation has now been reconstructed as well as in Fig. 7, and the combination of the two sets of great-circle paths resulted in a better resolution of the actual width of the perturbation. All inversion results in Figs 5 to 8 have a similar total model roughness, which makes a comparison among the models meaningful.

### 3.2 Global model of small-scale discontinuity undulations

The results of the previous section show the resolution that can be obtained with underside reflection data. However, existing data sets (for example Shearer 1993; Gossler & Kind 1996) have a more complete coverage of epicentral distances

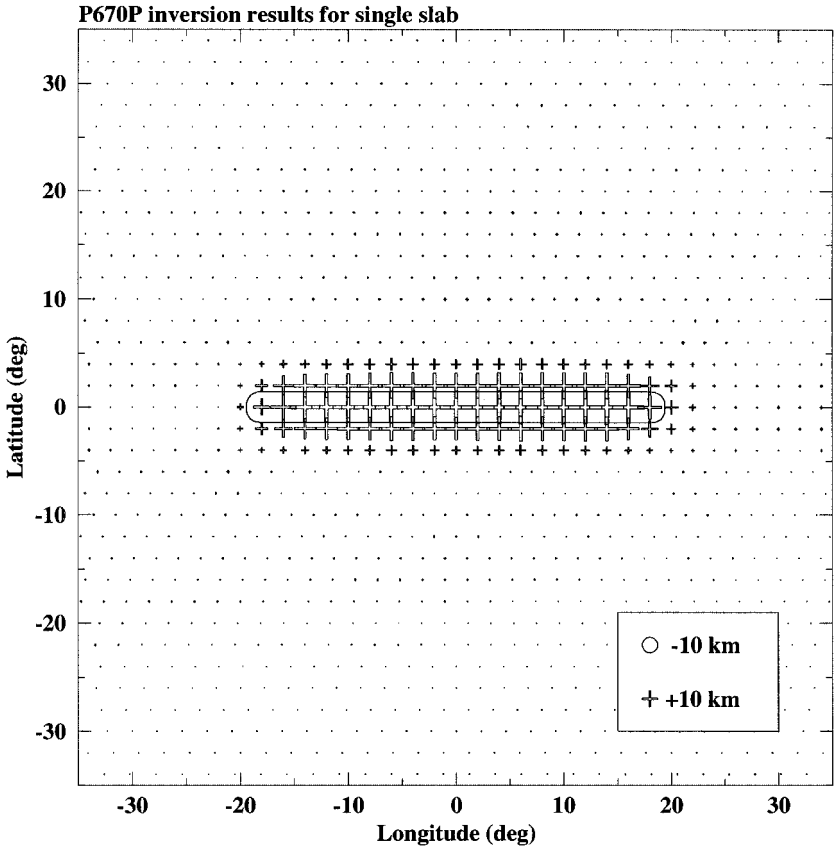


**Figure 7.** As Fig. 6, with the discontinuity perturbation rotated by 90°; source–receiver great circles now run parallel to the discontinuity structure. Depth variations in the model are between −1 and 22 km.

and great-circle azimuths and a more irregular spacing of $P_dP$ or $S_dS$ bounce points. These characteristics may result in an even better resolution of small-scale topographic features on the discontinuities. To assess the power of current data sets in reproducing small-scale discontinuity topography, a more realistic data set is generated. The data-set structure used is that of the data set of Shearer (1993), who collected high-quality transverse components of WWSSN stations, containing *SS* and precursors $S_dS$. The locations of the 5596 underside reflections and the local azimuths of the great circles at the bounce points are shown in Fig. 9. The global coverage of the data set is quite good, with a large number of reflections in the northwestern Pacific, but a rather limited coverage of the southern parts of South America and Africa. It is expected that the resolution of small-scale variations in the depth of the discontinuities is best in the northwest Pacific.

The model of slab-induced discontinuity perturbations used in the previous section is applied to all subduction zones on the globe to produce a map of global small-scale discontinuity-depth variations (thick grey lines in Fig. 9). Again, the depth variations for the 420- and 670-km discontinuities di er only in the sign of the depth perturbation. With this discontinuity depth model, $P_{420}P$ and $P_{670}P$ waveforms are computed for all bounce-point locations in Fig. 9. Traveltime and amplitude variations are again obtained with multi-channel cross-correlation.

Fig. 10 shows the apparent depth patterns obtained from the $P_{420}P$ synthetics. The traveltimes have again been converted to apparent discontinuity-depth perturbations, using the local derivative of traveltime with respect to discontinuity depth. Only the apparent depth perturbations with absolute values larger than 0.5 km are shown. As in the previous section, traveltime and amplitude (not shown) are a ected for bounce points far from the subduction zones, illustrating the large size of the Fresnel zone. Both positive and negative apparent depth variations are observed for bounce points near a subduction zone, which is a result of the mini-max nature of the waves. The traveltimes in Fig. 10 exhibit strong variations for closely spaced bounce points, with some huge outliers. These outliers are caused by strong focusing by topography on the 420-km discontinuity far from the geometrical bounce point, as explained in Section 2. If the traveltime of such waves is interpreted directly in terms of discontinuity depth, apparent discontinuities near 300 or 500 km depth would result. The $P_{420}P$ amplitudes are generally lower than expected for a 1-D earth. This illustrates that most of the energy that hits the subducting slabs is scattered and does not reach the receiver.

Apart from a few outliers, the traveltime data do not indicate strong non-linearity; that is, traveltime perturbations are smaller than the dominant period. Therefore, a 1-D (spherically symmetric) reference model is used in the inversion. Before the inversion, the outliers are removed from the data set, as they will dominate the misfit function and produce artefacts in the result. In this case, any apparent depth perturbation of more than 50 km is assumed to be an outlier. Fig. 11 shows the trade-o curve between data misfit and model roughness. Amplitude and traveltime data are weighted to have equal *a priori* rms misfit.

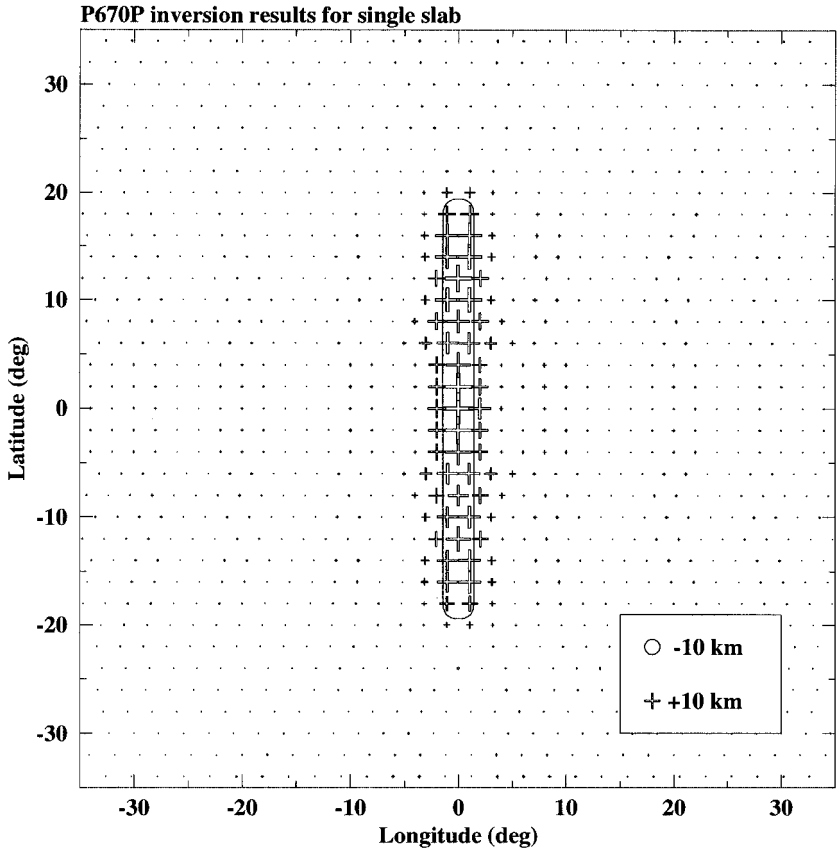


**Figure 8.** As Fig. 6, with the inversion performed with the data sets used for both Fig. 6 and Fig. 7 (crossing great-circle paths, both parallel and perpendicular to the discontinuity structure). Depth variations in the model are between −2 and 20 km.

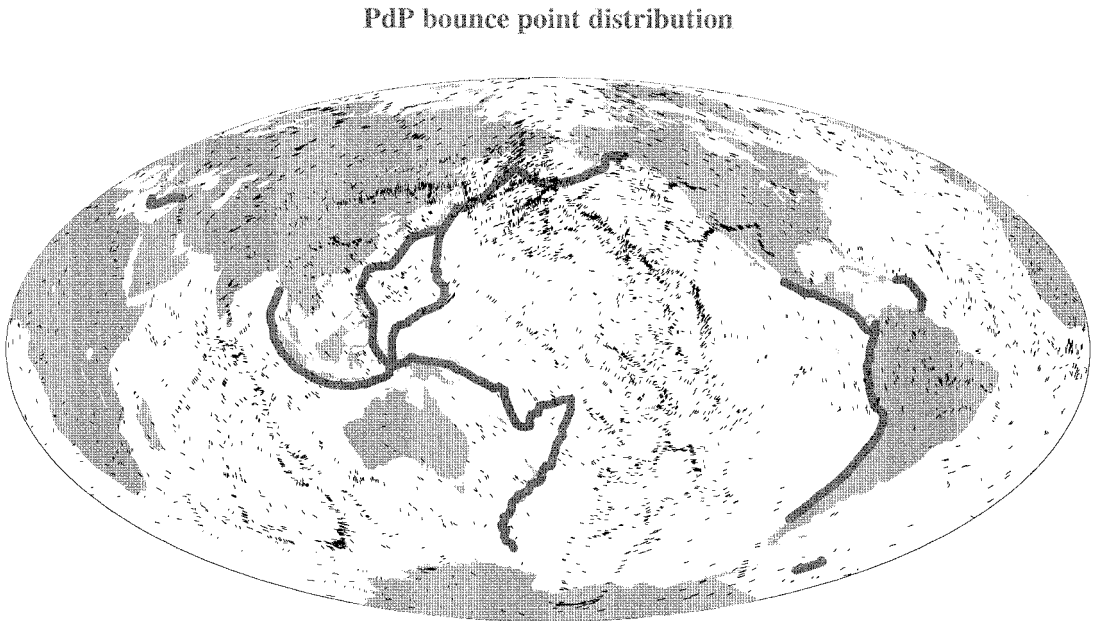


**Figure 9.** Distribution of bounce points in the synthetic data sets used in figures 10–18. A short dash at each bounce point gives the local orientation of the source-receiver great circle. The dark grey lines indicate the position of the subducting slabs used in forward modeling.

Fig. 12 shows the model represented by the solid circle in Fig. 11. The location of the subducting slabs is reconstructed well, but the height of the discontinuity elevation is too small (50 km in the true model, but only 10 km along most of the subduction zones). The figure shows that the subduction zones in the northwest Pacific are reconstructed well, as are the Java and the smaller Caribbean subduction zones. Side lobes that are present near the subduction zones are due to the

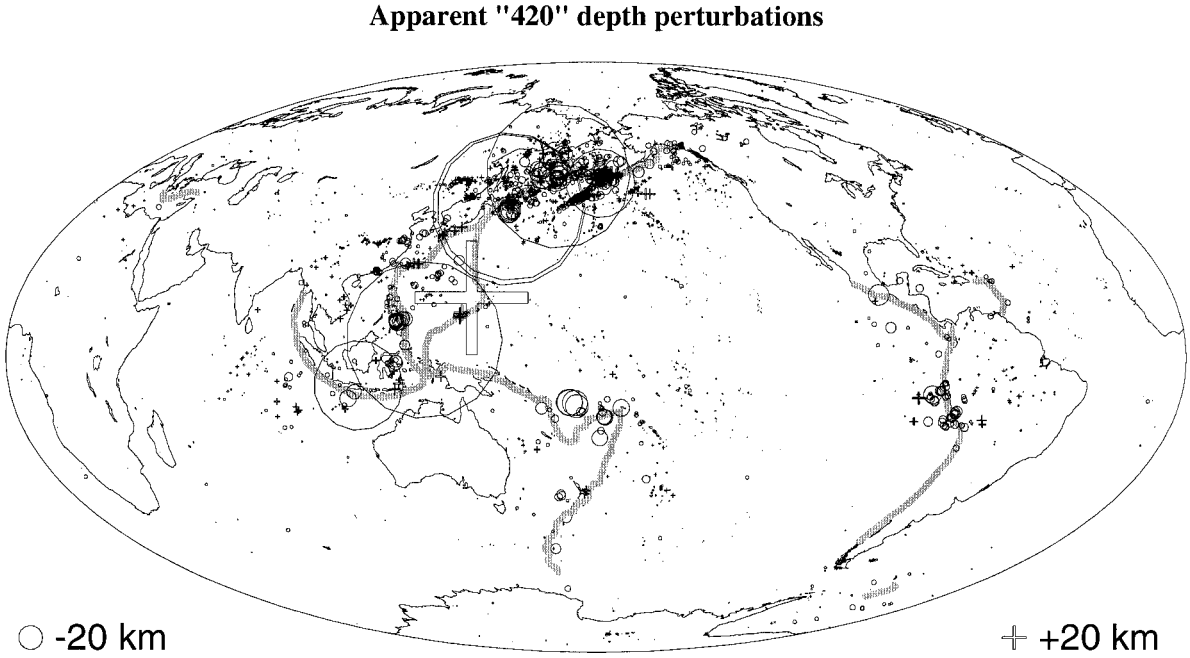


**Figure 10.** Apparent discontinuity-depth perturbations obtained from synthetic $P_{420}P$ data, for the data set shown in Fig. 9. Note that near the subduction zones both positive and negative apparent depth perturbations are found, with several outliers (defined as apparent depth perturbations of more than 50 km).

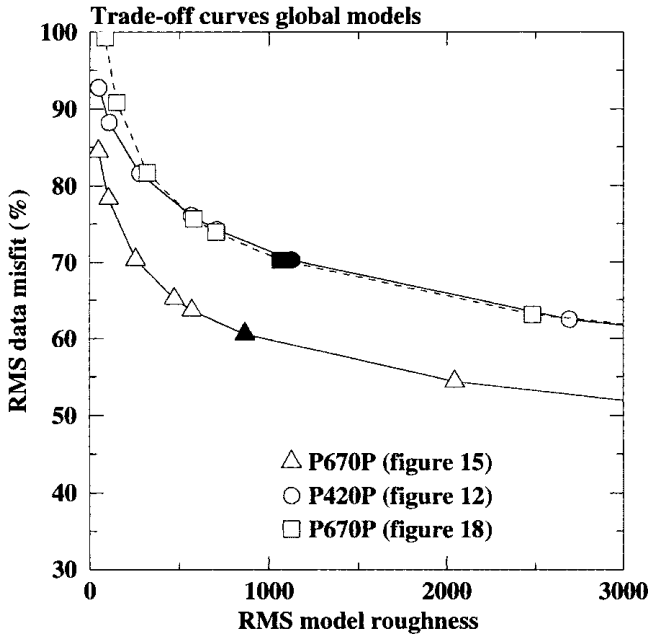


**Figure 11.** Trade-o curves of data misfit versus model roughness for the $P_{420}P$ and $P_{670}P$ data sets. The dashed line represents the trade-o curve for the 'egg-box plus subduction zones' model in Figs 17 and 18. The solid symbols represent the models shown in Figs 12, 15 and 18.

regularization constraints. In those regions where the data coverage is poor, the subduction-zone structure is not resolved well and artefacts appear, as, for example, in the west Pacific and along the South American coast.

The value of the inversion method used here can best be understood by comparing it with the more straightforward method that is currently used for underside-reflection data. In his studies of upper-mantle discontinuity topography, Shearer (1993) binned his observations into caps of 10° radius, assigning to the discontinuity depth at the centre of the cap the mode of the distribution in depths in the cap. This process of data reduction implicitly assumes that underside reflections are minimum-time arrivals, by ignoring the variations in the sensitivity kernel across the Fresnel zone. The method should produce valid results for undulations with scale lengths larger than the size of the Fresnel zone, since in that case the entire wavefield is delayed or advanced, but does not work for small-scale variations. Shearer's method can be viewed as an inversion of traveltime data only; the size of the averaging window or cap radius is the parameter that controls the roughness of the resulting model.

As an approximation of that method, the average of the data in Fig. 10 is computed over a $20° \times 20°$ moving window. The outliers are removed prior to averaging. The size of this area approximates the size of the dominant Fresnel zone in the data. No weight function across this area has been used. The di erence between the running average and running mode is negligible. The results in Fig. 13 show that the signal from the subduction zones is averaged to almost zero in many regions (notably the northwest Pacific, where data coverage is high); the method produces a low-passed version of the South American subduction-zone structure. Strong, long-wavelength artefacts are produced in some areas, such as those near the Indonesian and New Guinea arcs. These artefacts have the same magnitude as the depth variations in the models of Shearer (1991, 1993) and are due only to not using the proper sensitivity kernel in the inversion procedure. The results in Fig. 12 prove that, when the appropriate weight function across the Fresnel zone is used and amplitude and traveltime data are combined, the resolution obtained can be much higher than expected from the size of the Fresnel zone of the employed waves. A small-scale feature such as the Caribbean subduction

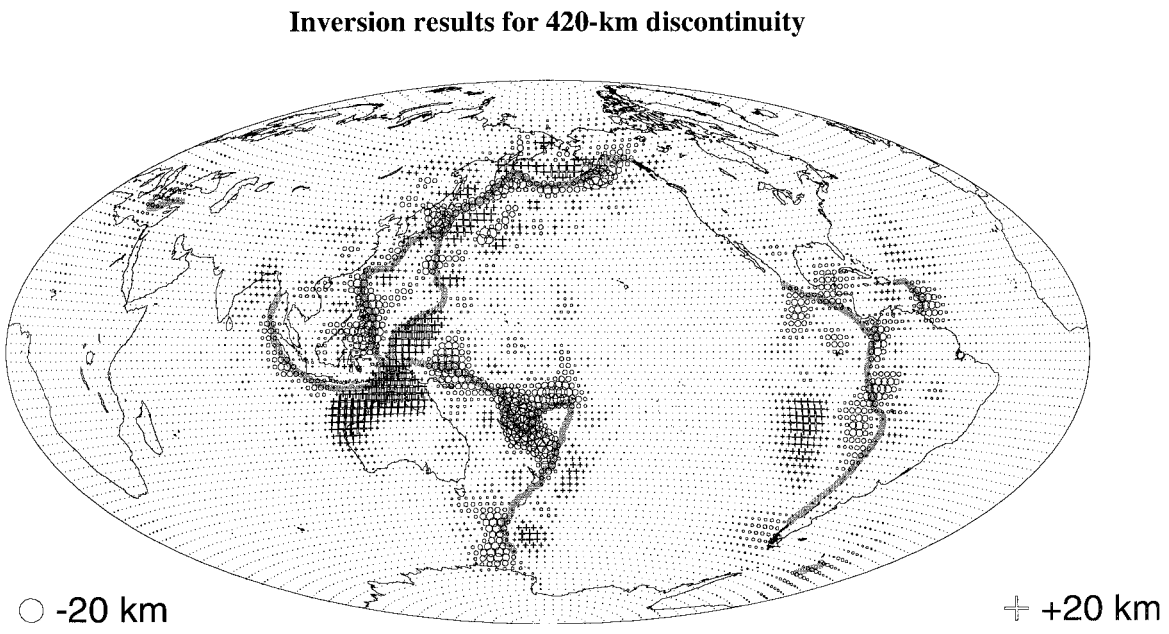


**Figure 12.** Model obtained from inversion of synthetic $P_{420}P$ data. Depth variations range from $-20$ km to $+17$ km. Well-resolved subduction zones are found in the northwest Pacific, where data coverage is high. Note that the Caribbean subduction zone is also resolved in the inversion. Artefacts near subduction zones are due to poor data coverage (East Pacific, north of Australia) and regularization constraints.

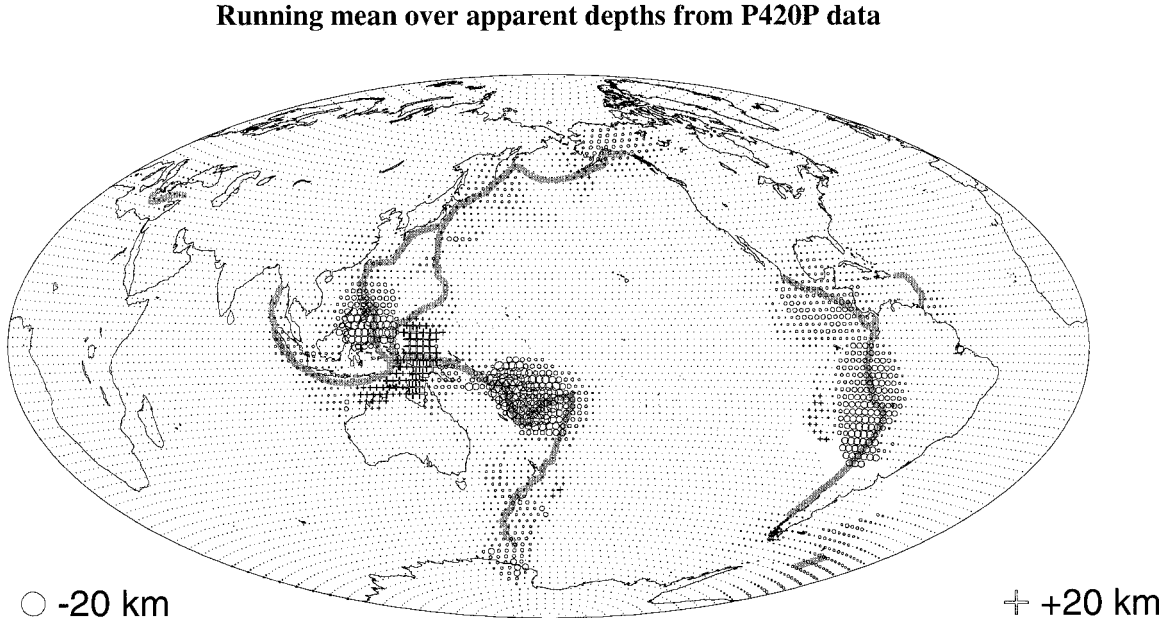


**Figure 13.** Running $20^\circ \times 20^\circ$ spatial average over the apparent depths in Fig. 10. This figure represents the result obtained with the currently used method of inverting $P_dP$ data. The signal from most subduction zones is averaged to zero (northwest Pacific) or converted to long-wavelength discontinuity undulations. Depth variations are between $-13$ and 10 km.

zone is retrieved in Fig. 12, whereas in Fig. 13 (the inversion of traveltimes only) all small-scale features have been mapped onto long-wavelength structure.

The same procedure as above is applied to $P_{670}P$ waves, synthesized for a model of expected slab-induced 670 km discontinuity-depth variations (for simplicity, assuming that all subducting slabs penetrate the 670-km discontinuity). This model di ers only in the sign of the depth variations from the model in Fig. 9. Traveltime data (converted to apparent depth) obtained from synthetic $P_{670}P$ data are presented in Fig. 14; amplitude data for this model are similar to those for the $P_{420}P$ waves and are not shown. Again, occasionally large traveltime perturbations are found, corresponding with large apparent depth variations (large crosses in Fig. 14). Note that, in contrast with the results for the 420-km discontinuity (Fig. 10), positive apparent depth perturbations dominate in the figure, especially in regions where many great-circle paths intersect the subducting slabs more or less at right angles. This is in line with the results of Davis *et al.* (1989), who showed that a downward deflection along the great-circle path focuses

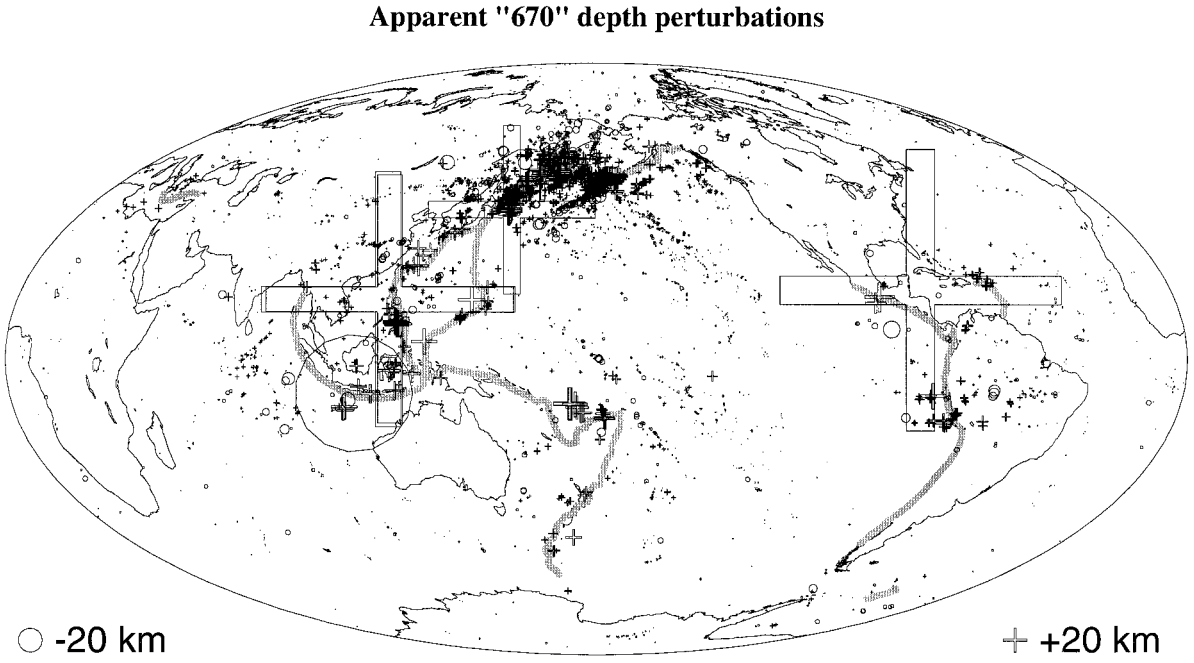


**Figure 14.** As Fig. 10, now for $P_{670}P$ data.

underside-reflected energy more e ciently than an uplift of the discontinuity. As noted by Neele *et al.* (1997), for this relatively narrow topographic structure the early arrivals correspond with energy focused by the shoulders of the slab-induced deflection. This energy arrives a few seconds ahead of the reference arrival time. (For the 420-km discontinuity uplift, the shoulders of the elevation defocus $P_{420}P$ energy. The remaining wavefield is then on average late, which explains the late arrivals—and negative apparent depths—in Fig. 10 for bounce points very close to the Aleutian Trench.)

The model represented by the solid triangle in Fig. 11 is shown in Fig. 15. The input model (Fig. 9) is reconstructed more completely than with the $P_{420}P$ data (Fig. 12). Strong artefacts are present near the Indonesian Arc, but only few data are available in that region. The South American, Aleutian and West Pacific subduction zones are reconstructed well. A smaller feature such as the Caribbean arc is present in the inversion result, but its position is not resolved well. Side lobes next to some of the subduction zones are due to poor data coverage. The absolute value of the discontinuity-depth perturbations along most subduction zones is again not reconstructed well (around 10 km).

For comparison, the result of computing the $20^\circ \times 20^\circ$ running average over the apparent depths in Fig. 14 is shown

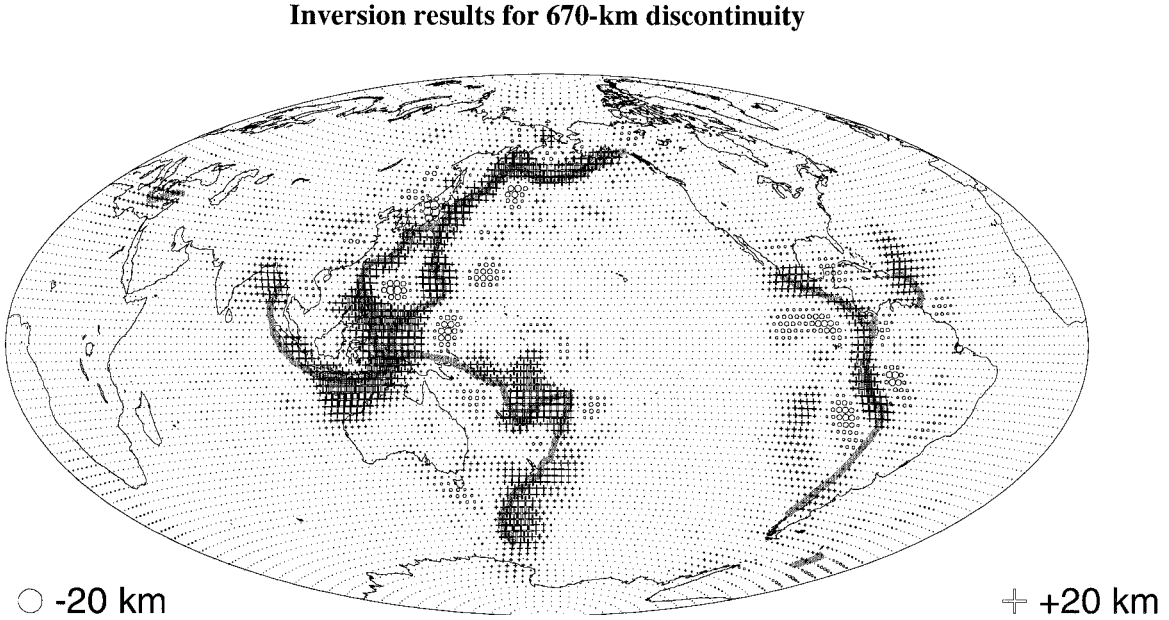


**Figure 15.** As Fig. 12, now for $P_{670}P$ data. Depth variations are between $-8$ and 16 km. Most subduction zones are reconstructed well, including those in areas with low data coverage.

in Fig. 16. Again, the small-scale subduction-zone-related deflections are mapped into large-scale apparent undulations of the discontinuity, with amplitudes between −7 and +17 km. This is of the same size as the peak-to-peak amplitudes found by Shearer (1993). In this case, the traveltime data do not average to zero, but produce a large-scale apparent undulation for most subduction zones. The value of the inversion method presented here lies in the much higher spatial resolution that it obtains.

Both position and amplitude of the discontinuity undulations in Fig. 16 bear a strong resemblance to the global 670-km discontinuity depth variations presented by Shearer (1993). This result suggests that his model of long-wavelength discontinuity-depth variations is more likely to be a low-pass version of discontinuity-depth variations induced by subduction zones than a map of true long-wavelength variations of discontinuity depth.

### 3.3 Combination of large- and small-scale undulations

The results in Figs 12 and 15 show that small-scale variations can be successfully recovered from long-period underside-reflection data, which is a major improvement over currently used imaging methods. To test the method further, a model containing both small- and large-scale undulations of the 670-km discontinuity is used to generate synthetics. The subduction zone model of Fig. 9 is superimposed on an egg-box-like topography, with a scale length of 60° in both latitude and longitude, and a peak-to-peak height of 10 km. A single extremum in the model thus measures about 30° across, which is larger than the size of the dominant Fresnel zone of the data.

As the $P_{670}P$ traveltime perturbations induced by this model are small (about 2 s for the egg-box) compared with the dominant period of 20 s, the present inversion method could be applied directly to these data. However, here a two-step inversion method is used. First, the running average over the apparent depths obtained from the traveltimes is performed, to obtain a model of large-scale depth variations of the discontinuity. This ensures that non-linearities in the remaining traveltime misfits are small. [The approximation (2) breaks down for large-amplitude undulations on the discontinuity on a scale larger than the size of the Fresnel zone, as in that case the errors associated with the linearization in (2) in each cell in the Fresnel zone add in phase.] This model contains artefacts as described above, but explains the large-scale traveltime variations in the data. Using the model as reference, the method presented here is applied to the remaining data misfit. The result is a model which contains small-scale features, if required by the data, and large-scale variations that were already present in the starting model. It is likely that some of the artefacts introduced in the first stage of this process remain present in the final model. To some extent, this is inevitable. The running-average method breaks down at small length scales, while the Kirchho -based method does not handle large-scale, large-amplitude depth variations well. In the two-stage process, these shortcomings are largely cancelled, with artefacts remaining for scale lengths comparable to the size of the Fresnel zone. This problem can be alleviated by using broad-band data and collecting traveltime and amplitude data for di erent bandpass filters applied to the waveforms. This introduces di erent Fresnel zone sizes in the data, which helps suppress the artefacts.

Fig. 17 shows the model obtained after computing the running spatial average over apparent depth perturbations. Zero crossings of the egg-box model are given by solid lines at constant latitude and longitude. The egg-box pattern of the true model is reconstructed well, including the peak-to-peak amplitude. The large-scale topography is retrieved well by simple averaging of the traveltime data over an area comparable with the Fresnel zone of the waves employed, in regions where no small-scale structure is present. Artefacts from the subduction-zone-related structure can be observed north of Australia and, though less clearly, in the northwest Pacific. Part of the structure from Fig. 16 can be recognized in Fig. 17, for example north of Australia and in the northwest Pacific.

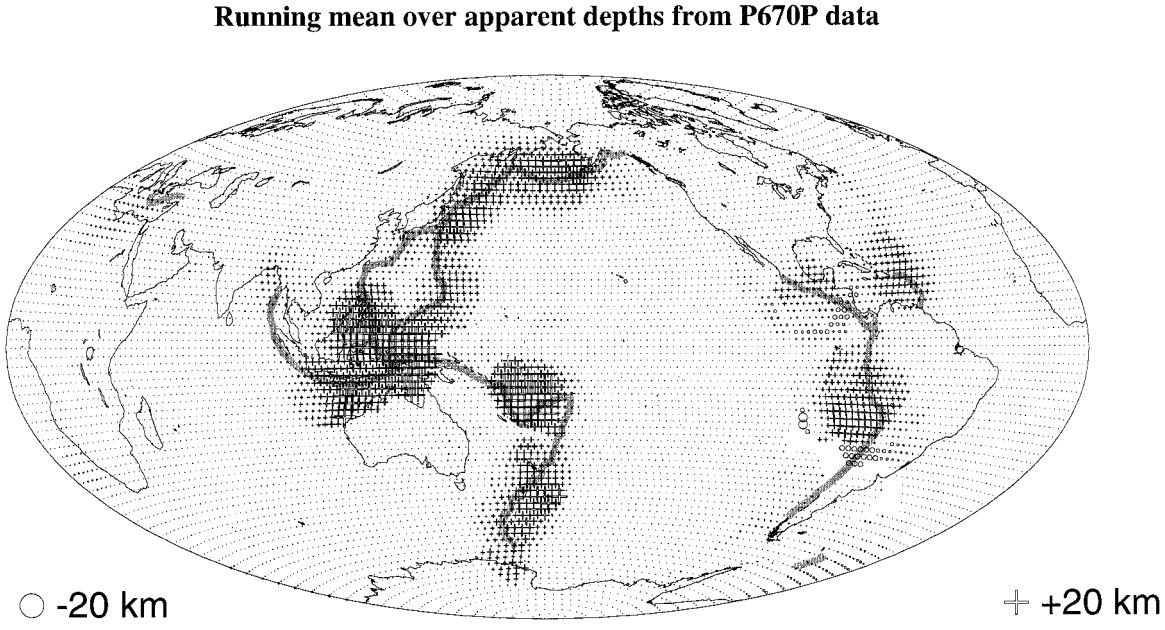


**Figure 16.** As Fig. 13, now for $P_{670}P$ data. Depth variations are between −7 and 18 km.

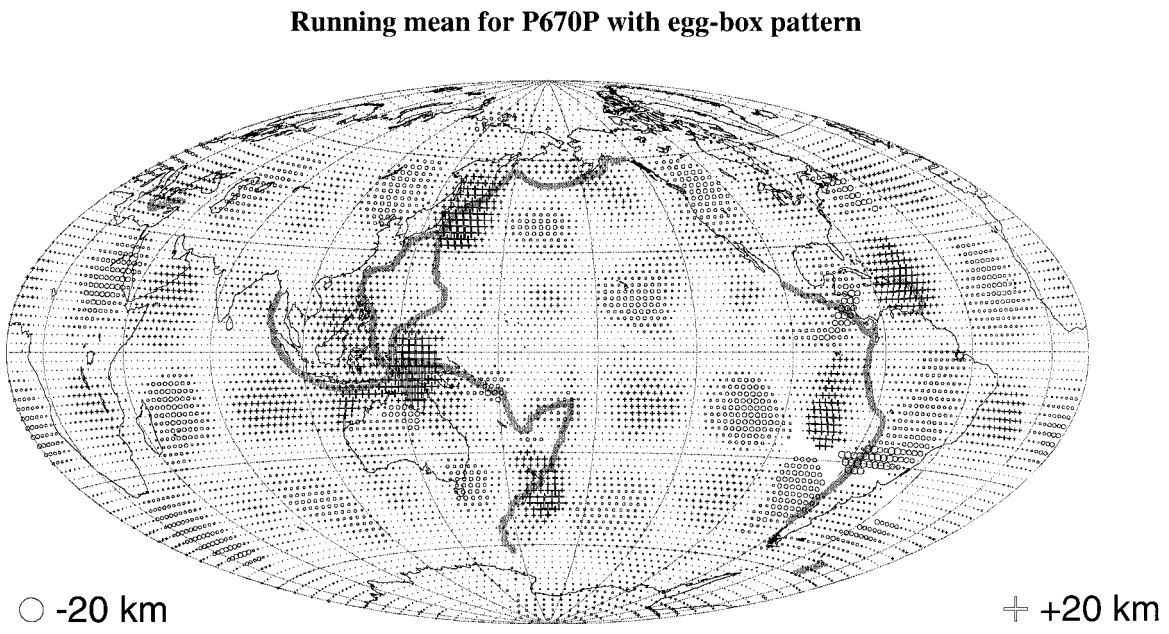


**Figure 17.** As Fig. 13, now for a model of 670-km discontinuity-depth variations described by an egg-box structure (wavelength 60°, peak-to-peak amplitude 10 km), superimposed on the subduction-zone model. The egg-box model is reconstructed well in the simple running-average process.

The inversion method is now applied to the data that remains unexplained by the 2-D reference model. The system of equations (10) to be solved is slightly altered, due to the non-zero curvature in the starting model. Minimizing the curvature in the final model, rather than the roughness of the model perturbation, (10) becomes

$$\begin{pmatrix} \gamma_A \mathbf{F}_a \\ \gamma_T \mathbf{F}_t \\ \gamma \partial_\theta^2 \\ \gamma \partial_\phi^2 \end{pmatrix} \boldsymbol{\delta h} = \begin{pmatrix} \gamma_A \Delta \log \mathbf{A} \\ \omega \gamma_T \Delta \mathbf{T} \\ -\gamma \partial_\theta^2 \mathbf{h}_0 \\ -\gamma \partial_\phi^2 \mathbf{h}_0 \end{pmatrix}, \tag{11}$$

where $\boldsymbol{\delta h}$ is the perturbation from the 2-D starting model $\mathbf{h}_0$. The (log-)amplitude and traveltime misfits $\Delta \log \mathbf{A}$ and $\Delta \mathbf{T}$ now also refer to the 2-D starting model.

The model represented by the solid dot along the trade-o curve for the 2-D reference model in Fig. 11 is shown in Fig. 18. This model has a total smoothness similar to that of the model in Fig. 17 (also shown in Fig. 11). The inversion of that part of the data unexplained by the running-average model hardly a ects the large-scale egg-box structure, but greatly improves the image of the subduction zones. The subduction zones do not appear as clearly as in Fig. 15, due to the signal from the large-scale structure, for example near Tonga. Where data

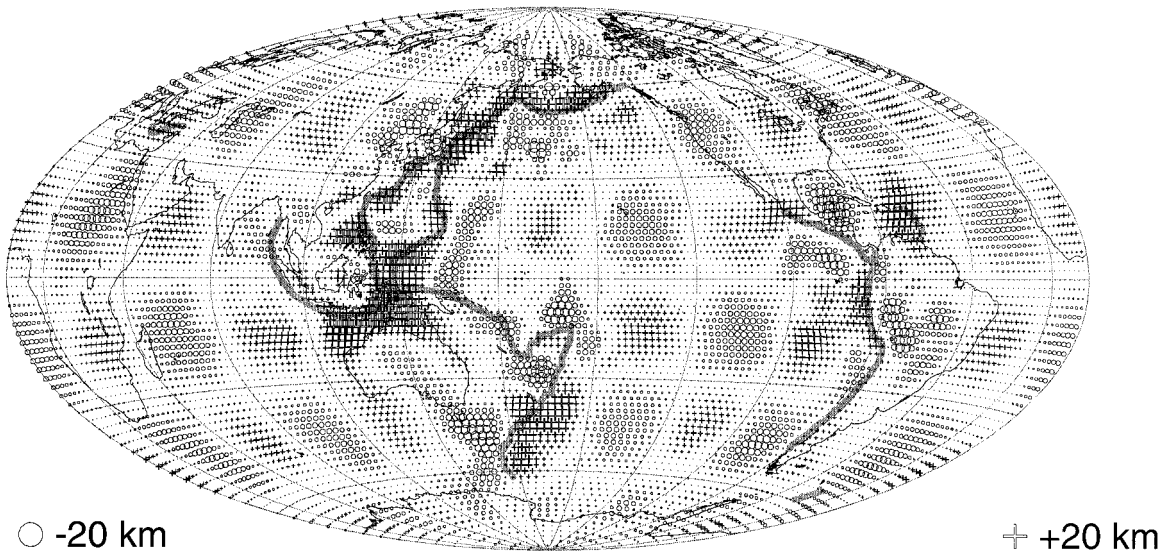


**Figure 18.** Inversion result of the $P_{670}P$ data from the 'egg-box plus subduction zones' model, using the model in Fig. 17 as reference. Depth variations are between −11 and 19 km.

coverage is high (northwest Pacific), the subduction zones are resolved well. Artefacts from the 2-D reference model can still be found, for example north of Australia. A comparison between Figs 15 and 18 shows that in Fig. 18, without the large-scale structure, the subduction-zone model is reconstructed as well as in Fig. 15.

## 4 AMPLITUDES VERSUS TRAVELTIMES

The present inversion method requires both amplitude and traveltime data. Although amplitude data can in principle be obtained from the *PP* or *SS* precursory wavetrain by cross-correlation methods, the standard error in these data is probably much larger than the error associated with traveltime data. An inversion of amplitudes and traveltimes with weights based on these standard errors may then completely downweight the amplitudes, resulting in an inversion of the traveltime data alone. Such an inversion reduces to a spatial averaging of the traveltime data, with a weight function across the Fresnel zone. The result of such an inversion is again a low-passed version of the true discontinuity topography; the model smoothness constraint controls the sharpness of the features in the result. Only when amplitude data are included in the inversion are scale lengths smaller than the Fresnel zone resolved. This once more illustrates the fact that amplitude data are sensitive to the first- and higher-order (spatial) derivatives of Earth structure. This is in agreement with the use of amplitude data in traveltime tomography, where the amplitude data constrain the higher derivatives of the velocity field (for example Neele *et al.* 1993a; Snieder & Lomax 1996).

## 5 DISCUSSION

A method is presented for retrieving lateral variations of the depth of upper-mantle discontinuities from traveltimes and amplitudes of underside reflections. The method is a major improvement over currently used imaging techniques, and the results show that it is possible to resolve structure on a scale smaller than the size of the Fresnel zone (but larger than the wavelength) of the waves used. This small-scale structure is retrieved by combining information from closely spaced wave paths and from amplitude data. It is shown that in this process it is essential to use the proper complex-valued weight functions on the reflecting interface. When a constant-valued function is used, as is done in current imaging techniques for underside reflections, a low-passed version of the true interface undulations is obtained, in which the spectral leakage of small-scale structure may seriously affect the resolution of true large-scale undulations.

Both large- and small-scale variations may be obtained in a combined approach, where the currently used method (simple averaging of traveltime data over an area comparable in size to the first Fresnel zone) is employed to find a smooth model of large-scale depth variations. The data that remain unexplained by this model (that is, that part of the traveltime data from small-scale discontinuity topography and the amplitude data) are then inverted using the method presented here. This approach combines the power of existing imaging methods at large scale lengths with the ability of the present spectral method to resolve details on a scale smaller than the size of the Fresnel zone. It is expected that, for scale lengths comparable to the size of the dominant Fresnel zone in the data, artefacts remain present in the final results. These artefacts should be largely removed by using broad-band data; that is by combining data with different dominant frequencies.

The Fréchet derivatives of spectrum perturbations due to interface displacements are derived using a linearization of the phase term in the Kirchhoff-integral representation of the wavefield. This restricts the application of the method to low-amplitude interface undulations. However, the method allows for a relatively simple quasi non-linear inversion, as the Fréchet derivatives can be computed with respect to any smooth reference model. In this way, large traveltime and amplitude perturbations may be inverted iteratively. These reference models are required to be smooth, as the Kirchhoff formulation used here is valid only for small curvatures of the interface.

Volume heterogeneities have been ignored in the present formulation of the inverse problem. Although these, if present, contribute to traveltime perturbations, discontinuity undulations are more effective in producing traveltime variations. For example, a 3 per cent velocity variation over a length of 300 km is needed to produce the same traveltime perturbation as that from a discontinuity displaced over only 6 km. Volume heterogeneities, as well as interface displacements were accounted for by Vasco *et al.* (1995), in their global inversion of *P*, *PP*, *S*, *SS* traveltimes and $SS-S_dS$ differential traveltimes for upper- and lower-mantle structure. However, these authors failed to take the mini-max nature of underside reflections into account, causing artefacts in the discontinuity topography in their results.

The method requires both traveltime and amplitude data. Although this introduces the difficulty of collecting and handling amplitude data, current data processing techniques yield the necessary information. Shearer (1993) computed the cross-correlation between the *SS* precursors and the *SS* waveform. Both traveltime and amplitude of any *SS* precursor can be obtained from the resulting correlograms. The data in eq. (10) are then the differential traveltime $SS-S_dS$, and amplitude ratio $A_{S_dS}/A_{SS}$. Forward modelling can be used to account for the effect of surface topography on the *SS* waveform.

The method could also be used with traveltimes alone, if amplitude data were not available. The inversion then reduces to a spatial average over the data, similar to the currently used method to image discontinuity-depth variations. However, because of the physically more exact weight function across the Fresnel zone, the maps of discontinuity undulations that would be obtained with the method presented here would show a sharper image of small-scale structure. The amplitude data nevertheless contain the information on the higher spatial derivatives of the discontinuity structure, and the best results are obtained when amplitude data are included in the inversion.

The examples presented in this paper show the problems associated with a straightforward interpretation of traveltimes of underside reflections in terms of discontinuity depth at or near the bounce point. Focusing of wave energy scattered far from the ray-geometrical bounce point may lead to arrivals in the seismogram that may have amplitudes larger than that of the geometrical underside reflection and strongly deviating traveltimes. The examples presented here show that if such arrivals are interpreted as regular underside reflections, discontinuities near 300, 500 or 800 km could locally appear to exist. Previous studies have pointed out other problems associated with the *PP* or *SS* precursory wavetrain. Schimmel & Paulssen (1997) showed that asymmetric underside reflections exist in a spherically symmetric earth. Not accounting for these

arrivals also could lead to incorrect discontinuity depths. If the $P_dP$ or $S_dS$ data are derived from cross-correlation using the *PP* of *SS* waveform, the observations of Paulssen & Stutzmann (1996) should be taken into account. These authors point out that interference from secondary arrivals may a ect the *PP* waveform. Such waveform perturbations may also cause incorrect identification of the precursory underside reflections and lead to erroneous discontinuity depths.

## ACKNOWLEDGMENTS

We acknowledge Peter Shearer for providing us with the event-station distribution of his 1993 data set. George Hel rich and Michael Weber are gratefully acknowledged for their constructive reviews. This research was supported by the Netherlands Organization for Scientific Research (NWO) through the Pionier project PGS 76-144. This work was conducted under the programme of the Dutch national research school, the Vening Meinesz Research School of Geodynamics.

## REFERENCES

Bleistein, N., 1984. *Mathematical Methods for Wave Phenomena,* Academic Press, Orlando.

Collier, J. & Hel rich, G., 1997. Topography of the '410' and '660' km seismic discontinuities in the Izu-Bonin subduction zone, *Geophys. Res. Lett.,* **24,** 1535–1538.

Davis, J.P., Kind, R. & Sacks, I.S., 1989. Precursors to P′P′ re-examined using broad-band data, *Geophys. J. Int.,* **99,** 595–604.

Doornbos, D.J., 1992. Di raction and seismic tomography, *Geophys. J. Int.,* **108,** 256–266.

Forte, A.M. & Woodward, R.L., 1997. Seismic-geodynamic constraints on 3D structure, flow, and heat transfer in the mantle, *J. geophys. Res.,* **102,** 17 981–17 994.

Frazer, L.N., 1987. Synthetic seismograms using multifold path integrals—I. Theory, *Geophys. J. R. astr. Soc.,* **88,** 621–646.

Frazer, L.N. & Sen, M.K., 1985. Kirchho –Helmholtz reflection seismograms in a laterally inhomogeneous multi-layered elastic medium—I. Theory, *Geophys. J. R. astr. Soc.,* **80,** 121–147.

Gossler, J. & Kind, R., 1996. Seismic evidence for very deep roots of continents, *Earth planet. Sci. Lett.,* **138,** 1–13.

Groenenboom, J. & Snieder, R., 1995. Attenuation, dispersion and anisotropy by multiple scattering of transmitted waves through distributions of scatterers, *J. acoust. Soc. Am.,* **98,** 3482–3492.

Hel rich, G.R., Stein, S. & Wood, B.J., 1989. Subduction zone thermal structure and mineralogy and their relationship to seismic wave reflections and conversions at the slab/mantle interface, *J. geophys. Res.,* **94,** 753–763.

Ito, E. & Takahashi, E., 1989. Postspinel transformations in the system $Mg_2SiO_4$–$Fe_2SiO_4$ and some geophysical implications, *J. geophys. Res.,* **94,** 10 637–10 646.

Kampfmann, W. & Muller, G., 1989. *PcP* amplitude calculations for a core-mantle boundary with topography, *Geophys. Res. Lett.,* **16,** 653–656.

Luo, Y. & Schuster, G.T., 1991. Wave-equation traveltime inversion, *Geophysics,* **56,** 645–653.

Neele, F. & Snieder, R., 1992. Topography of the 400 km discontinuity from observations of long-period P400P phases, *Geophys. J. Int.,* **109,** 670–682.

Neele, F., VanDecar, J. & Snieder, R., 1993a. A formalism for including amplitude data in tomographic inversions, *Geophys. J. Int.,* **115,** 482–496.

Neele, F., VanDecar, J. & Snieder, R., 1993b. The use of *P*-wave amplitude data in a joint inversion with traveltimes for upper-mantle velocity structure, *J. geophys. Res.,* **98,** 12 033–12 054.

Neele, F., de Regt, H. & VanDecar, J., 1997. Gross errors in upper-mantle discontinuity topography from $P_dP$ or $S_dS$ data, *Geophys. J. Int.,* **129,** 194–204.

Niu, F. & Kawakatsu, H., 1995. Direct evidence for the undulation of the 660-km discontinuity beneath Tonga: Comparison of Japan and California array data, *Geophys. Res. Lett.,* **22,** 531–534.

Nowack, R.L. & Lyslo, J.A., 1989. Frechet derivatives for curved interfaces in the ray approximation, *Geophys. J.,* **97,** 497–509.

Paige, C.C. & Saunders, M.A., 1982. LSQR: an algorithm for sparse linear equations and sparse least squares, *ACM Trans. Math. Soft.,* **8,** 195–209.

Paulssen, H. & Stutzmann, E., 1996. On PP–P di erential traveltime measurements, *Geophys. Res. Lett.,* **23,** 1833–1836.

Phipps-Morgan, J. & Shearer, P., 1993. Seismic constraints on mantle flow and topography of the 660-km discontinuity: evidence for whole-mantle convection, *Nature,* **365,** 506–511.

Ringdal, F., Husebye, E.S. & Dahle, A., 1972. Event detection problems using a partially coherent seismic array, *NTNF/NORSAR Rep. 45.*

Rodgers, A. & Wahr, J., 1993. Inference of core-mantle boundary topography from ISC PcP and PKP traveltimes, *Geophys. J. Int.,* **115,** 991–1011.

Schimmel, M. & Paulssen, H., 1996. Steeply reflected *ScSH* precursors from the D″ region, *J. geophys. Res.,* **101,** 16 077–16 087.

Schimmel, M. & Paulssen, H., 1997. Asymmetrically reflected PP and SS precursors: 2. A mechanism to generate non-stationary arrivals, in preparation.

Sen, M.K. & Frazer, L.N., 1987. Synthetic seismograms using multifold path integrals—II. Computations, *Geophys. J. R. astr. Soc.,* **88,** 647–671.

Shearer, P., 1990. Seismic imaging of upper mantle structure with new evidence for a 520-km discontinuity, *Nature,* **344,** 121–126.

Shearer, P., 1991. Constraints on upper mantle discontinuities from observations of long-period reflected and converted phases, *J. geophys. Res.,* **96,** 18 147–18 182.

Shearer, P., 1993. Global mapping of upper mantle reflectors from long-period SS precursors, *Geophys. J. Int.,* **115,** 878–904.

Shearer, P.M. & Masters, T.G., 1992. Global mapping of topography on the 660-km discontinuity, *Nature,* **355,** 791–796.

Snieder, R. & Lomax, A., 1996. Wavefield smoothing and the e ect of rough velocity perturbations on arrival times and amplitudes, *Geophys. J. Int.,* **125,** 796–812.

VanDecar, J.C. & Crosson, R.S., 1990. Determination of teleseismic relative phase arrival times using multi-channel cross-correlation and least squares, *Bull. seism. Soc. Am.,* **80,** 1049–1061.

Van der Lee, S., Paulssen, H. & Nolet, G., 1994. Variability of P660s phases as a consequence of topography of the 660 km discontinuity, *Phys. Earth planet. Inter.,* **86,** 147–164.

Vasco, D.W. & Majer, E.L., 1993. Wavepath traveltime tomography, *Geophys. J. Int.,* **115,** 1055–1069.

Vasco, D.W., Johnson, L.R. & Pulliam, J., 1995. Lateral variation in mantle velocity structure and discontinuities determined from *P, PP, S, SS* and *SS–SdS* traveltime residuals, *J. geophys. Res.,* **100,** 24 037–24 059.

Vidale, J.E. & Benz, H.M., 1992. Upper-mantle seismic discontinuities and the thermal structure of subduction zones, *Nature,* **356,** 678–682.

Woodward, M.J., 1992. Wave-equation tomography, *Geophysics,* **57,** 15–26.